energies

Article

A Ring-Shaped Curved Deformable Self-Powered Vibration Sensor Applied in Drilling Conditions

Hu Wang [1], He Huang [2], Chuan Wu [3,*] and Jinrun Liu [3]

1 111 Geological Brigade of Guizhou Provincial Bureau of Geology and Mineral Resources, Guiyang 550081, China
2 Powerchina Hubei Electric Engineering Co., Ltd., Wuhan 430040, China
3 Faculty of Mechanical and Electronic Information, China University of Geosciences, Wuhan 430074, China
* Correspondence: wuchuan@cug.edu.cn

Abstract: Because of their low flexibility, traditional vibration sensors cannot perform arbitrary bending adjustments when facing curved surfaces and other complex working conditions during the drilling process; therefore, this research proposes a ring-shaped vibration sensor (RSV−TENG) that can deform freely in the bending direction, and which can be used in working conditions where the inner bending angle of the drill pipe changes greatly. Test results show that the vibration frequency measurement range is from 4 Hz to 16 Hz, with a measurement error less than 4%, the vibration amplitude measurement range is less than 20 mm, with a measurement error less than 5%, the output voltage and current signal are 120 V and 60 nA, respectively, when three RSV−TENGs are connected in parallel, and the maximum output power is 6×10^{-7} W when the external resistance is 10^6 Ω. Compared with traditional downhole sensors, this sensor has self-powered and self-sensing functions, eliminating the shortcomings of battery and cable power supply; in addition, this sensor can be installed in the drill pipe space with different curvature radii, so it is more suited to complex and changeable downhole working conditions.

Keywords: triboelectric nanogenerator; self-powered sensor; downhole vibration

Citation: Wang, H.; Huang, H.; Wu, C.; Liu, J. A Ring-Shaped Curved Deformable Self-Powered Vibration Sensor Applied in Drilling Conditions. *Energies* **2022**, *15*, 8268. https://doi.org/10.3390/en15218268

Academic Editors: Wenjian Yang and Huawei Chang

Received: 16 September 2022
Accepted: 3 November 2022
Published: 5 November 2022

1. Introduction

During the drilling process, vibration is selected as a carrier to carry the specific information of the state of the drilling tool and downhole working conditions, which can provide reference to drilling monitoring and operational control [1]. At present, the methods of collecting downhole vibration information mainly include measurement while drilling (MWD, LWD) [2,3], surface measurement system to measure vibration [4], triaxial accelerometer [5,6], dynamic model prediction [7], and so on, but the main problem studied in this paper is that the installation of the sensor is limited [8,9] due to the thin diameter and bendability of the drill pipe; that is, when the curvature radius of the drill pipe is large, traditional sensors cannot be used because they cannot bend; meanwhile, curvature, as a key indicator of directional deviation correction, determines whether the drilling trajectory meets expectations. Therefore, it is necessary to develop a vibration sensor that can be freely deformed in the curved direction, which can be freely bent according to the curvature of the curved surface, and which can bypass other drilling equipment inside the drill pipe to obtain the vibration information of the drill string at this stage.

In addition, the power-supply method of the downhole sensors mostly contains cables and batteries, but the cable power-supply method leads to a more difficult construction, while the battery method leads to frequent drilling and is not conducive to drilling. In order to improve drilling efficiency, a new power-supply method is needed to reduce the burden of the traditional power-supply method and even replace it.

The triboelectric nanogenerator (TENG) proposed in 2012 has been widely applied in the fields of sensors and generators [10,11]. In the sensors field, research results have been achieved regarding speed sensors [12,13], pressure sensor [14,15], vibration sensor [16–18], human motion sensors [19,20], and so on. In the generators field, research results have been achieved regarding energy harvesting and the collection and reuse of various energies, such as blue energy [21], human motion energy [22,23], and environmental mechanical energy [24–26]. Some scholars have also conducted research on self-powered downhole sensors [27–29], which also provides a basis for the application of triboelectric nanogenerators to downhole vibration measurement; based on this, a ring bending deformation self-powered vibration sensor (RSV−TENG) suitable for downhole conditions is proposed in this study. The sensor can bend freely according to the curvature of the surface, solving the problem of limited installation, and applying the self-powered method.

2. Structural Design and Working Principle

2.1. Structural Design

The main body of the annulus-like curved deformable sensor (RSV−TENG) consists of an internal spherical vibration sensor. As shown in Figure 1a, the internal vibration sensor is composed of a casing, copper electrodes, PTFE balls, and a counterweight. The structure of the whole sensor is spherical, consisting of a shell, two copper electrodes, Teflon balls, and a counterweight. We used the 3D printing process to produce the acrylic board. Each spherical shell is divided into two parts. An acrylic plate is installed inside the two spherical shells. The upper acrylic adhering section is copper electrode 1, the face of positive, and the bottom acrylic adhering section is copper electrode 2, the same size as copper electrode 1, and the face of negative. The PTFE balls are placed between the two copper electrodes. The counterweight is placed under copper electrode 2 in the lower shell to ensure the directionality and stability of the sensor. Finally, the current is led out through wires and connected to the electrometer to form a loop. The sensor housing is constructed of PMMA with a diameter of 50 mm, the diameter of each copper electrode is 43 mm with a thickness is 0.05 mm, and the diameter of each inner PTFE ball is 5 mm. During the subsequent tests, we placed 10 PTFE balls inside the sensor. The bottom counterweight is a steel ball with a diameter of 10 mm and a counterweight of 10 g.

2.2. Working Principle

Figure 1b is the schematic cross-sectional view of the vibration sensor. Due to the effect of the counterweight, the direction of the internal spherical vibration sensor is always consistent, no matter how the RSV−TENG is bent or deformed, which effectively improves the accuracy of the sensor measurements. The working principle of the sensor is introduced in combination with Figure 1c. In the initial state shown in Figure 1c(i), the PTFE ball is in contact with copper electrode 2 because of gravity, and the PTFE attracts negative charges on the surface of the lower copper electrode and, thus, negatively charges the overall material due to the difference in the ability of PTFE and copper to gain and lose electrons. In order to cause the entire system to reach potential balance, the surface of copper electrode 2 is positively charged, and the potential difference is 0 at this state. As shown in Figure 1c(ii), when the drill string vibrates the PTFE ball produces an upward force and separates from copper electrode 2 due to the inertial force. Since the PTFE is a polymer material, its negative charge is not easily lost, so it will not break the system.

The balance of potentials will create a potential difference, causing copper electrode 1 to attract electrons to copper electrode 2, which will generate a current in the external circuit. When a PTFE ball moves to copper electrode 1, as shown in Figure 1c(iii), the positive charges of copper electrode 2 have all been transferred to copper electrode 1, and balance is again reached. When a PTFE ball moves downward again to the state shown in Figure 1c(iv), the balance is again broken, and the electrons of copper electrode 1 return to copper electrode 2, so a reverse current is generated in the external circuit until equilibrium is again reached.

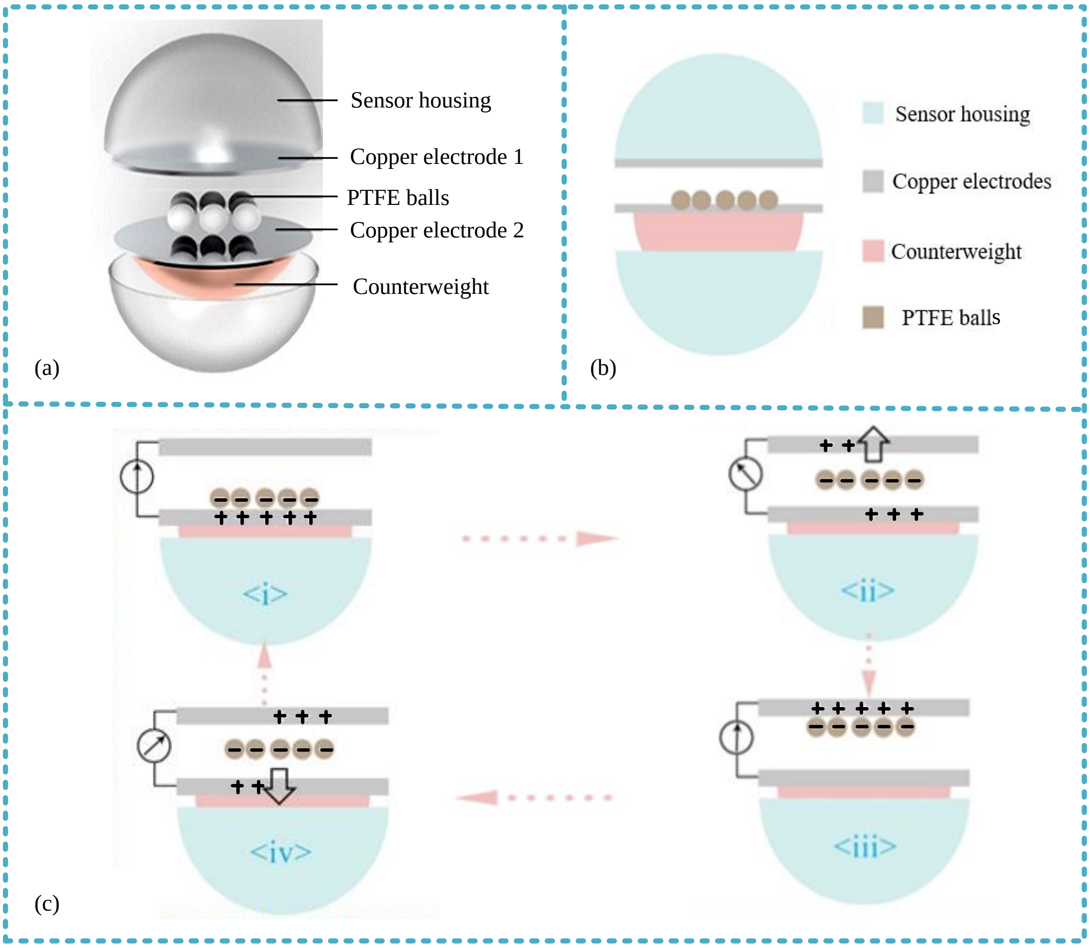

Figure 1. Internal structure and working principle of the RSV−TENG. (**a**,**b**) are the two-dimensional cross-sectional view of the ring-shaped deformable sensor; and (**c**) the working principle of the ring-shaped deformable sensor.

3. Sensor Performance Tests

Figure 2 shows the physical image of RSV−TENG and the structure of the internal sensor. As shown in Figure 2a, the sensor can be installed in a ring-shaped casing, and the internal spherical sensor can be freely increased or decreased according to the actual working conditions. The RSV−TENG provides better flexibility in the bending position where the drill pipe will inevitably bend during drilling, and is more suited to drilling in inclined and trenchless wells. In order to more easily observe whether the counterweight of the internal sensor can play a role in stability, as shown in Figure 2b, we used a link casing with higher transparency and flexibility for tests and demonstrations. The test results showed that no matter how the link casing transforms, its counterweight would play a role, so that the direction of the sensor always maintains an upward state.

3.1. Sensing Performance Tests

Firstly, the vibration frequency and amplitude of the sensor were tested. When sensors were installed inside the pipe, under the effect of the counterweight the sensors always stayed in the same horizontal plane as the PTFE balls. The drill pipe vibrated during the process of drilling, and the PTFE pellets with the copper electrodes in relative motion under the effect of inertia resulted in mass implementation of different friction contact between the separating electrodes; thus, potential difference was generated, and the voltage pulse signal could be detected after the circuit was formed by the external wire, so that the real-time vibration frequency could be obtained by analyzing and calculating the voltage pulse signal. It can be seen from Figure 3a that the number of voltage pulses and voltage per unit time increase with the increase of the frequency. The number of pulses per unit time was 9 with a voltage amplitude of 90 V when the vibration frequency was 9 Hz, and the number of pulses per unit time was 16 with a voltage amplitude of 137 V when the vibration frequency was 16 Hz, so it is feasible to calculate the real time frequency by the number of pulses per unit time. It can be seen from the 6 Hz waveform diagram that the pulse peak was composed of multiple small peaks rather than a smooth straight line because the inner PTFE ball was composed of multiple balls in the structural design of the sensor; therefore, the output waveform was created by each small PTFE ball hitting the surface of the copper electrode, and the peak of its pulse was composed of multiple small peaks.

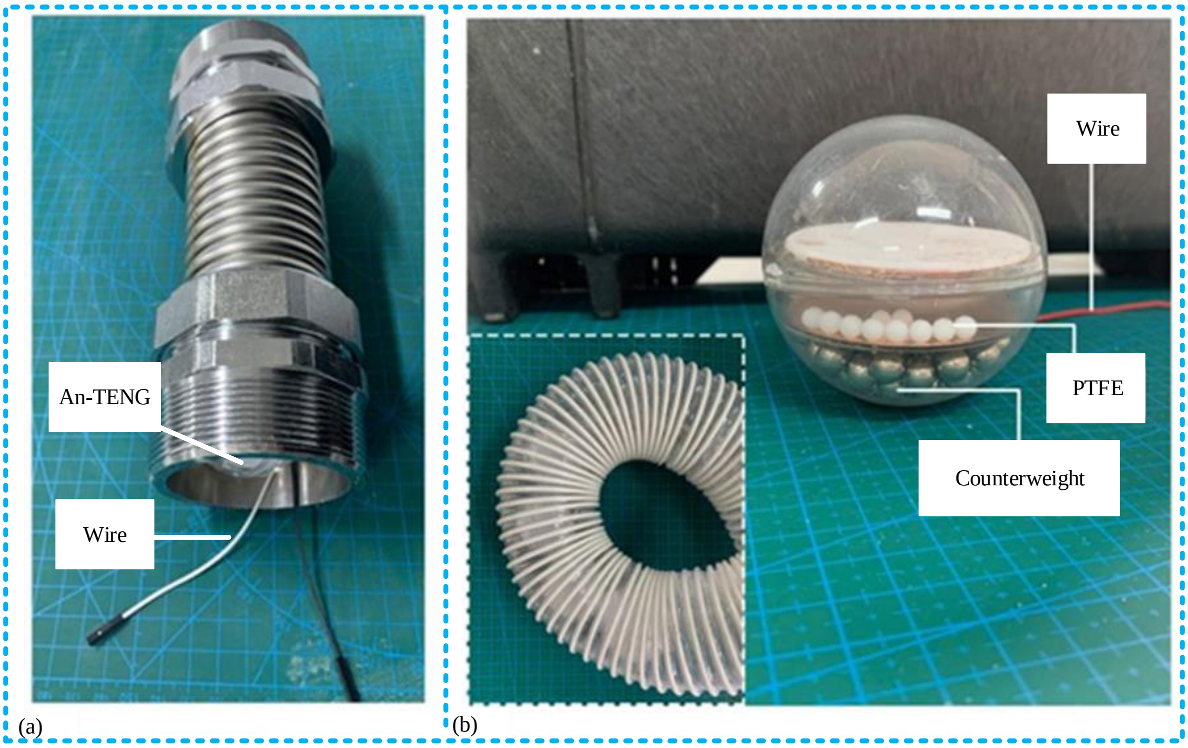

Figure 2. A physical image of the RSV−TENG. (**a**) A physical installation image of the RSV−TENG; and (**b**) the structural diagram of the internal sensor of RSV−TENG.

Next, the amplitude measurement performance of the sensor was tested. In this research, the frequency of 6 Hz was selected for tests, and only the single variable amplitude was measured. The results showed that the amplitude of the sensor was proportional to the voltage, and the voltage output between different amplitudes had a large difference. For example, the voltage generated by the amplitude of 15 mm was 22 V higher than the voltage generated by the amplitude of 10 mm. When the vibration frequency was 20 mm, the output voltage reached the maximum value of 100 V, and when the amplitude continued to increase by more than 25 mm, the output voltage remained at 100V, which may have been due to inadequate contact. The vibration frequency measurement range of the sensor was in the range of 0 to 16 Hz, and the measurement error was kept within 4% (see Figure 3c), and the RSV−TENG could measure the vibration amplitude with a measurement range of 0 to 20 mm and a measurement error less than 5% (see Figure 3d).

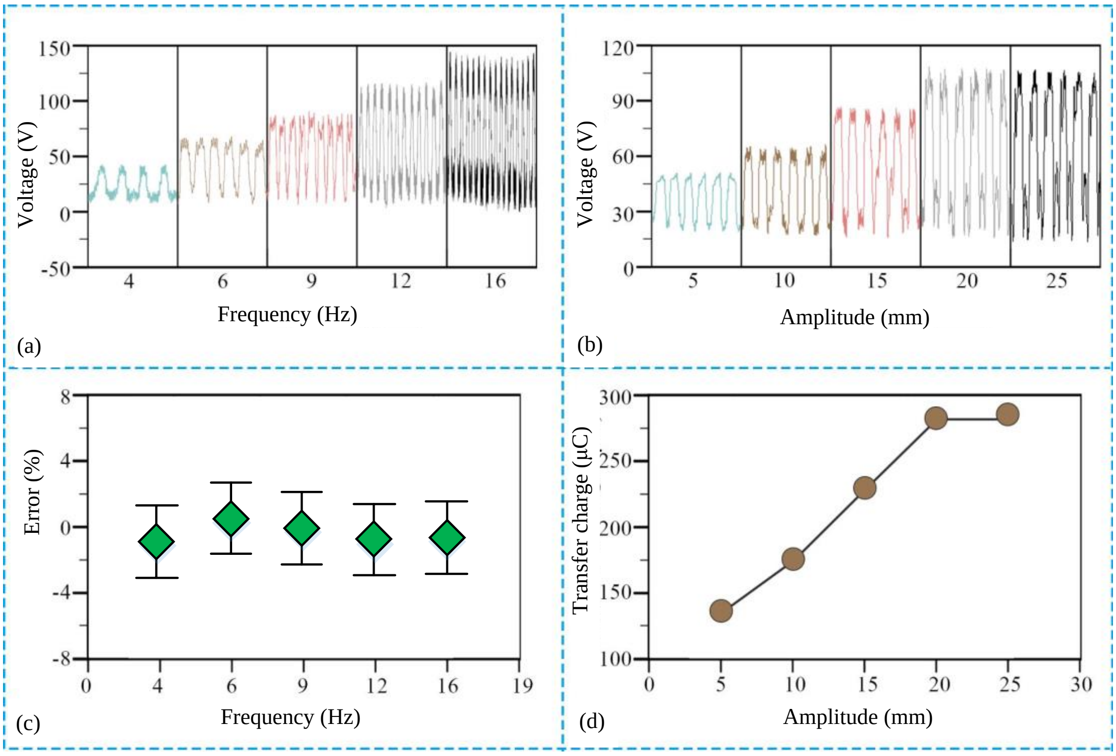

Figure 3. Sensing performance study of the RSV−TENG. (**a**) Frequency−sensing performance; (**b**) amplitude−sensing performance; (**c**) vibration frequency measurement error; and (**d**) vibration amplitude measurement error.

Secondly, the reliability of the sensor was tested. As shown in Figure 4a,b, the output voltage of RSV−TENG still remained within the normal range when the sensor was working 4500 times. Subsequently, tests were carried out on the bending angle of RSV−TENG, and the results shown in Figure 4b show that the output voltage of the sensor remained the same no matter how the angle of the sensor changed, indicating that the counterweight could stabilize the sensor direction and output voltage inside the sensor. During the bottom hole measurement, the internal spherical sensing unit randomly appeared in any angle of the curved deformation when the annular casing was deformed in the curved direction, and the test results showed that it would not affect the output performance of the internal spherical sensing unit no matter any curved deformation of the RSV−TENG, so the RSV−TENG could connect any internal spherical sensor unit to measure the vibration state of the drill string, which further improved the reliability of the sensor.

The working environment of the sensor was then tested. In these tests, the vibration frequency range of 4 Hz to 12 Hz was selected as an example for the tests in order to get closer to actual working conditions. For every 100 m increase in the drilling depth, the formation temperature would increase by 3 °C, so we measured the working state of the sensor in a high-temperature environment and the results are shown in Figure 4c. The results show that the output voltage of each frequency of the sensor was stable and did not change significantly with the increase in temperature, so the sensor could continue to work at high temperature and could adapt to the high-temperature underground environment. Finally, the output performance of the sensor in different humidity environments was tested and the results shown in Figure 4d show that the output voltage of the sensor at different frequencies was still stable with the increase in ambient humidity, which proved that the sensor was also suitable for working environments with different humidities.

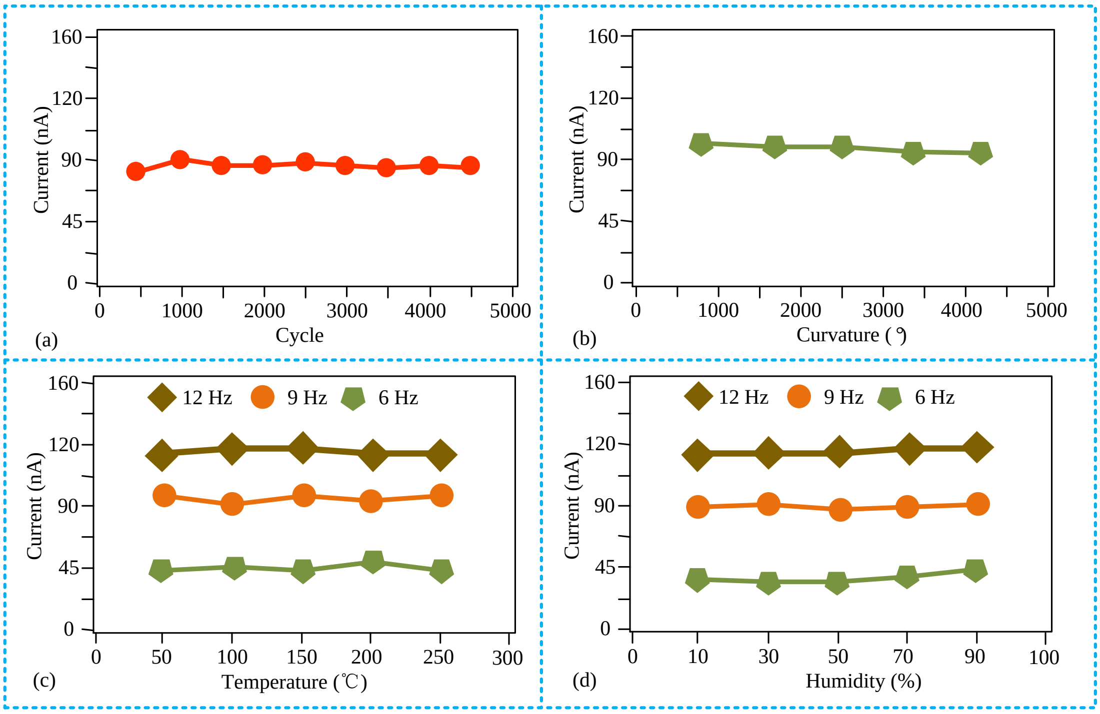

Figure 4. Sensing performance of the RSV−TENG. (**a**) Repeatability tests of the RSV−TENG; (**b**) long-time working tests of the RSV−TENG; (**c**) output performance of the RSV−TENG under different temperatures; and (**d**) output performance of the RSV−TENG under different humidity.

3.2. Power-Generation Performance Tests

The power-generation performance of RSV−TENG was studied with resistors of different resistance values. When there was only one vibration sensor inside RSV−TENG, it can be seen from Figure 5a that the voltage value of the sensor increased with the increase in vibration frequency and external resistance, and the growth area was divided into three stages. In the first stage, the resistance value was from 0 to 5.5×10^4 Ω, and the output voltage of a single sensor was always low, approaching 0. When the resistance value is from 5.5×10^4 to 10^7 Ω, the voltage was in the rising stage, and the output voltage of RSV−TENG in this stage had a linear positive correlation with the resistance value. In the third stage, the resistance value was from 10^7 to 10^9 Ω, and the voltage of each frequency in this stage tended to be stable and reached the highest value. At the same time, it could be seen from Figure 5 that when the vibration amplitude was 12 Hz, the voltage increase slope was more than 9 Hz and the voltage increase slope was more than 4 Hz. The output of the current under different resistance values was also measured, and the output could also be divided into three stages. In the first stage, when the output current was from 0 to 5.5×10^4 Ω, the output current remained stable and there was no obvious difference. The output value was the highest of the three stages; meanwhile, the rate of change increased with the increase in frequency.

When the frequency was 12 Hz, the output current reached the maximum value of 20 nA. When the second stage was from 5.5×10^4 Ω to 10^7 Ω, the output current value dropped sharply. When it reached the third stage, the output current of RSV−TENG was the smallest and approached 0. In these three stages, the current output reached the minimum value. Finally, the output power of RSV−TENG with only a single vibration sensor inside was calculated, and the results show that the output power could reach a maximum of 6×10^{-7} W when the resistance was 10^6 Ω and the vibration frequency was 12 Hz.

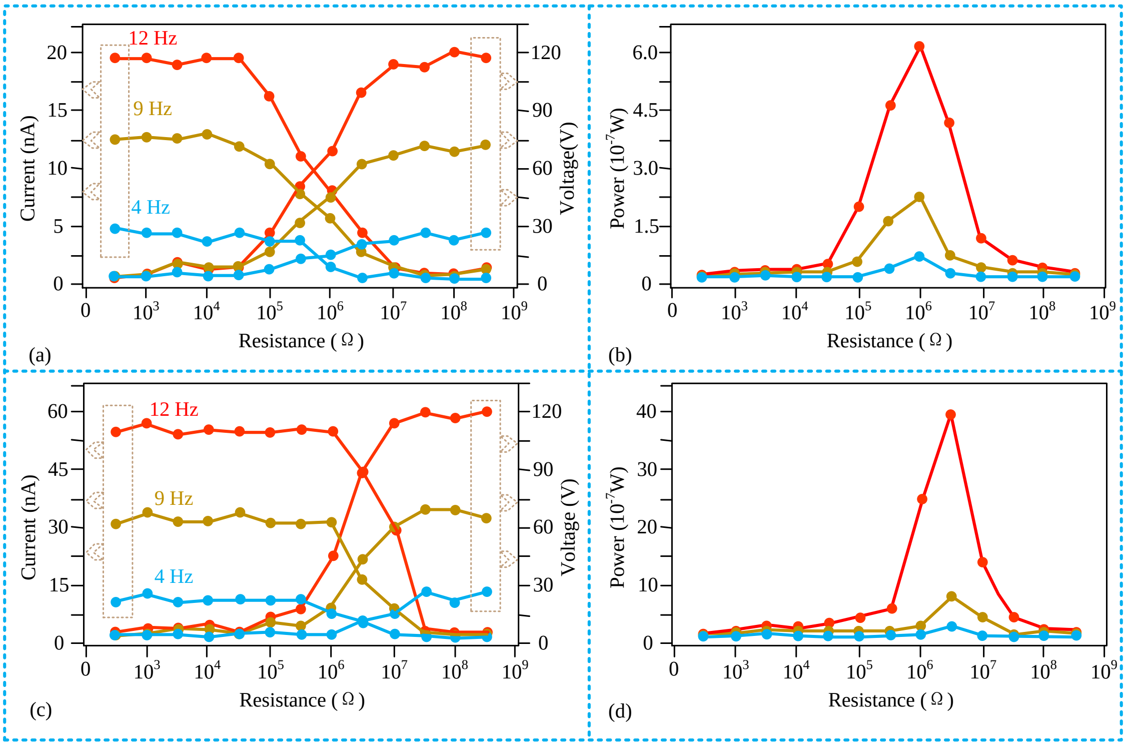

Figure 5. Power-generation performance of the RSV−TENG. (**a**) Output voltage and current of a single RSV−TENG under different external resistances; (**b**) output power of a single RSV−TENG under different external resistances; (**c**) output voltage and current of three RSV−TENGs under different external resistances; and (**d**) output power of three RSV−TENGs under different external resistances.

Finally, three vibration sensors were installed in the ring-shaped casing and were tested, and the results showed that the output voltage of a single sensor could reach 120 V when the vibration frequency was 12 Hz, which proved that three vibration sensors connected in parallel would increase the output signal. As shown in Figure 5c,d, when the three sensors were connected in parallel, the output voltage did not increase significantly, but the output current increased significantly. When the external circuit was connected to different resistances, the resistance drop was still divided into three stages. The first stage was in the range of 0 to 10^6 Ω. The current change speed in this stage was slow and stable, and the output value was the highest, that is, the output current was 56 nA when the vibration frequency was 12 Hz; also from the current graph, it can be seen that the current drop slope at 12 Hz was significantly higher than the drop curves at 4 Hz and 9 Hz in the second stage. Finally, the output power of RSV−TENG containing multiple vibration sensors was calculated and the results showed that the output power could reach a maximum of 40×10^{-7} W when the resistance was 5.5×10^6 Ω and the vibration frequency was 12 Hz.

3.3. Influence of Internal Structure on Sensor Output Performance

As shown in Figure 3a, the peak value of the voltage waveform was not a smooth curve because of multiple PTFE balls, so it was necessary to conduct a detailed study and comparison of the number of PTFE balls in the internal structure. As shown in Figure 6a, there was only one peak with a peak of 10 V in the voltage waveform when there was only one PTFE ball in the internal structure, and the number of peaks in the voltage waveform increased to 5 with a peak of 50 V when there were 5 PTFE balls inside, so the number of PTFE balls also determined the output value of the voltage and the voltage was proportional to the number and volume of the PTFE balls. The relationship between the copper electrode area and the output voltage was then studied. As shown in Figure 6b, when the number of PTFE balls was determined, different copper electrode areas did not have much effect on the output performance. Compared with copper electrodes, the number and volume of PTFE balls determined the amount of triboelectric charge transfer inside the sensor. When the number of PTFE balls increased, the amount of triboelectric charge transfer inside the sensor also increased, thereby increasing the output voltage of the sensor; therefore, the vibration state of the bottom hole drill string could be studied by selecting an appropriate number of PTFE balls according to actual working conditions. Finally, the distance between the two copper electrodes was studied. As shown in Figure 6c, the output voltage increased as the distance between the copper electrodes increased, but the output voltage reached the maximum value when the distance between the copper electrodes increased to 20 mm, so the optimal distance of the copper electrode was selected as 20 mm in order to achieve the best performance in the design of the sensor.

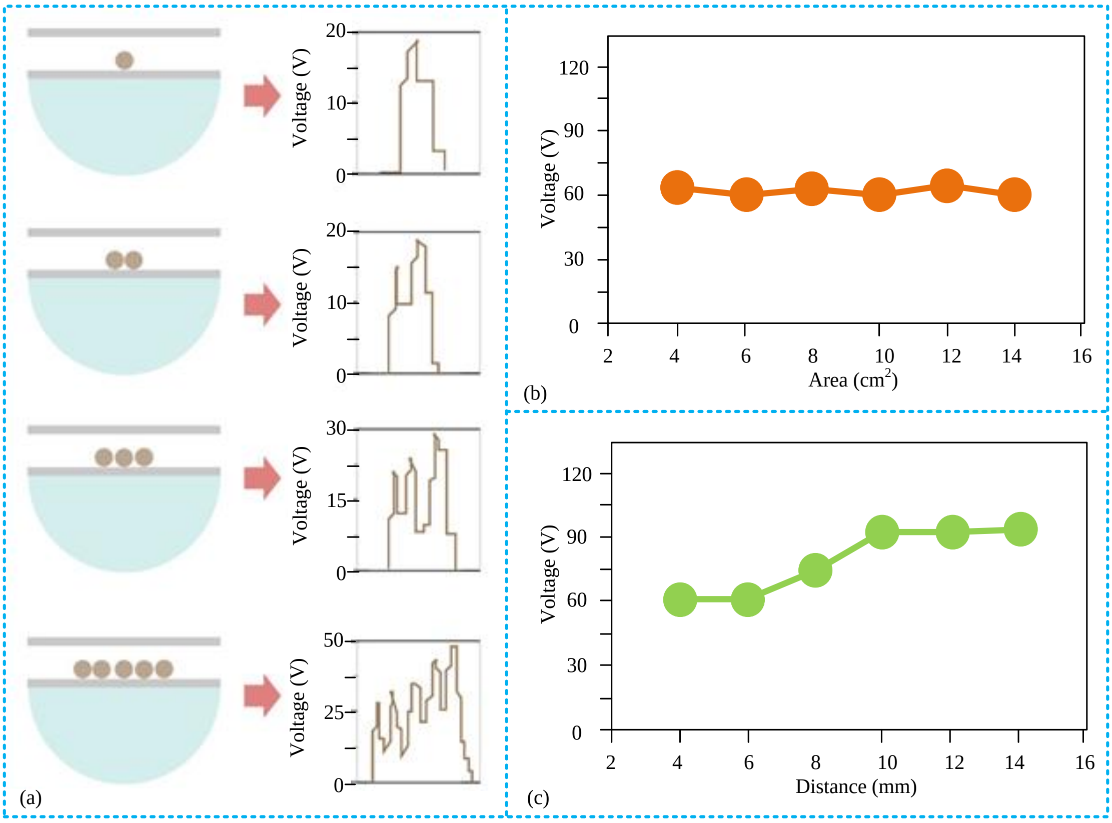

Figure 6. Influence of the internal structure on the output performance of the sensor. (**a**) Effect of the number of PTFE balls on the output voltage and waveform; (**b**) effect of the area of the copper electrode on the output performance of the sensor; and (**c**) effect of the distance of the copper electrode on the output performance.

4. Conclusions and Discussions

A ring-shaped vibration sensor (RSV−TENG) that can be freely deformed in bending direction is proposed in this research, and which can be used in the working environment where the bending angle of the drill pipe changes greatly. The vibration frequency measurement range is 4 Hz to 16 Hz with a measurement error within 4%, the measurement amplitude measurement range is 0 mm to 20 mm with a measurement error within 5%, and the measurement range can be improved by changing the structure and material subsequently. Meanwhile, the RSV−TENG with different curvatures was measured. The measurement results found that the RSV−TENG was less affected by the change of curvature and the environment of different temperature and humidity, which proved that the sensor could still work continuously and stably under complex working conditions. After running 4500 times, the sensor could still work normally, showing that the sensor has a high working life and reliability.

The output power of the sensor was measured and studied, and the results showed that the output voltage of a single sensor was as high as 120 V, and when three vibration sensors were connected in parallel, the output current could reach up to 60 nA. The maximum output power of a single sensor was 6×10^{-7} W when the external resistance was 106 Ω, while it was 40×10^{-7} W when three vibration sensors were connected in parallel and the external resistance was 5.5×10^{6} Ω, which provided a reference for self-powered sensors to power other components.

Author Contributions: Conceptualization, C.W.; methodology, C.W.; software, H.H.; validation, C.W.; formal analysis, C.W.; investigation, C.W.; resources, C.W.; data curation, J.L.; writing—original draft preparation, J.L.; writing—review and editing, J.L.; visualization, C.W.; supervision, C.W.; project administration, H.W.; and funding acquisition, H.H., H.W. All authors have read and agreed to the published version of the manuscript.

Funding: This work was supported by the Guizhou Province Science and Technology Support Program (2022-245); the Guangdong Basic and Applied Basic Research Foundation (2022A1515010467); the Geological Scientific Research Project of Guizhou Provincial Bureau of Geology and Mineral Exploration and Development (2021-25); and the Geological Survey Project of China Geological Survey (DD20211421).

Data Availability Statement: Not applicable.

Conflicts of Interest: The authors declare no conflict of interest.

References

1. Zha, Y.; Pham, S. Monitoring downhole drilling vibrations using surface data through deep learning. In *SEG Technical Program Expanded Abstracts 2018*; Society of Exploration Geophysicists: Houston, TX, USA, 2018; pp. 2101–2105.
2. Isheyskiy, V.; Sanchidrián, J.A. Prospects of applying MWD technology for quality management of drilling and blasting operations at mining enterprises. *Minerals* **2020**, *10*, 925. [CrossRef]
3. Lei, W.; Yiren, F.; Chao, Y.; Zhenguan, W.; Shaogui, D.; Weina, Z. Selection criteria and feasibility of the inversion model for azimuthal electromagnetic logging while drilling (LWD). *Pet. Explor. Dev.* **2018**, *45*, 974–982.
4. Okoli, P.; Cruz Vega, J.; Shor, R. Estimating Downhole Vibration via Machine Learning Techniques Using Only Surface Drilling Parameters. In *SPE Western Regional Meeting*; OnePetro: Richardson, TX, USA, 2019.
5. Wang, L.; Zhang, C.; Gao, S.; Lin, T.; Li, X. Influence of linear vibration on the errors of three-axis FOGs in the measurement while drilling systems. *Optik* **2018**, *156*, 204–223. [CrossRef]
6. Wang, C.; Liu, G.; Yang, Z.; Li, J.; Zhang, T.; Jiang, H.; Cao, C. Downhole working conditions analysis and drilling complications detection method based on deep learning. *J. Nat. Gas Sci. Eng.* **2020**, *81*, 103485. [CrossRef]
7. Zhang, H.; Di, Q.; Li, N.; Wang, W.; Chen, F. Measurement and simulation of nonlinear drillstring stick–slip and whirling vibrations. *Int. J. Non-Linear Mech.* **2020**, *125*, 103528. [CrossRef]
8. Zhao, G.F.; Di, W.N. Application Perspective of Environmentally Responsive Materials in the Downhole Operation. In *Materials Science Forum*; Trans Tech Publications Ltd.: Wollerau, Switzerland, 2020; Volume 993, pp. 799–805.
9. Sasaki, T.; Park, J.; Soga, K.; Momoki, T.; Kawaguchi, K.; Muramatsu, H.; Imasato, Y.; Balagopal, A.; Fontenot, J.; Hall, T. Distributed fibre optic strain sensing of an axially deformed well model in the laboratory. *J. Nat. Gas Sci. Eng.* **2019**, *72*, 103028. [CrossRef]
10. Wang, Z.L. Triboelectric nanogenerator (TENG)—Sparking an energy and sensor revolution. *Adv. Energy Mater.* **2020**, *10*, 2000137. [CrossRef]
11. Luo, J.; Gao, W.; Wang, Z.L. The triboelectric nanogenerator as an innovative technology toward intelligent sports. *Adv. Mater.* **2021**, *33*, 2004178. [CrossRef]
12. Wang, Y.; Yang, E.; Chen, T.; Wang, J.; Hu, Z.; Mi, J.; Pan, X.; Xu, M. A novel humidity resisting and wind direction adapting flag-type triboelectric nanogenerator for wind energy harvesting and speed sensing. *Nano Energy* **2020**, *78*, 105279. [CrossRef]
13. Zou, H.X.; Zhao, L.C.; Wang, Q.; Gao, Q.H.; Yan, G.; Wei, K.X.; Zhang, W.M. A self-regulation strategy for triboelectric nanogenerator and self-powered wind-speed sensor. *Nano Energy* **2022**, *95*, 106990. [CrossRef]
14. Zhao, Z.; Huang, Q.; Yan, C.; Liu, Y.; Zeng, X.; Wei, X.; Hu, Y.; Zheng, Z. Machine-washable and breathable pressure sensors based on triboelectric nanogenerators enabled by textile technologies. *Nano Energy* **2020**, *70*, 104528. [CrossRef]
15. Venugopal, K.; Panchatcharam, P.; Chandrasekhar, A.; Shanmugasundaram, V. Comprehensive review on triboelectric nanogenerator based wrist pulse measurement: Sensor fabrication and diagnosis of arterial pressure. *ACS Sens.* **2021**, *6*, 1681–1694. [CrossRef] [PubMed]

16. Wang, L.; He, T.; Zhang, Z.; Zhao, L.; Lee, C.; Luo, G.; Mao, Q.; Yang, P.; Lin, Q.; Li, X.; et al. Self-sustained autonomous wireless sensing based on a hybridized TENG and PEG vibration mechanism. *Nano Energy* **2021**, *80*, 105555. [CrossRef]
17. Teng, W.; Ding, X.; Tang, S.; Xu, J.; Shi, B.; Liu, Y. Vibration analysis for fault detection of wind turbine drivetrains—A comprehensive investigation. *Sensors* **2021**, *21*, 1686. [CrossRef]
18. Fang, L.; Zheng, Q.; Hou, W.; Zheng, L.; Li, H. A self-powered vibration sensor based on the coupling of triboelectric nanogenerator and electromagnetic generator. *Nano Energy* **2022**, *97*, 107164. [CrossRef]
19. Kim, Y.; Yun, J.; Kim, D. Robust and flexible triboelectric nanogenerator using non-Newtonian fluid characteristics towards smart traffic and human-motion detecting system. *Nano Energy* **2022**, *98*, 107246. [CrossRef]
20. Zaw, N.Y.W.; Yun, J.; Goh, T.S.; Kim, I.; Kim, Y.; Lee, J.S.; Kim, D. All-polymer waterproof triboelectric nanogenerator towards blue energy harvesting and self-powered human motion detection. *Energy* **2022**, *247*, 123422.
21. Jiang, T.; Pang, H.; An, J.; Lu, P.; Feng, Y.; Liang, X.; Zhong, W.; Wang, Z.L. Robust swing-structured triboelectric nanogenerator for efficient blue energy harvesting. *Adv. Energy Mater.* **2020**, *10*, 2000064. [CrossRef]
22. Zhu, M.; Yi, Z.; Yang, B.; Lee, C. Making use of nanoenergy from human–Nanogenerator and self-powered sensor enabled sustainable wireless IoT sensory systems. *Nano Today* **2021**, *36*, 101016. [CrossRef]
23. Park, D.; Hong, J.H.; Choi, D.; Kim, D.; Jung, W.H.; Yoon, S.S.; Kim, K.H.; An, S. Biocompatible and mechanically-reinforced tribopositive nanofiber mat for wearable and antifungal human kinetic-energy harvester based on wood-derived natural product. *Nano Energy* **2022**, *96*, 107091. [CrossRef]
24. Lu, H.; Zhao, W.; Wang, Z.L.; Cao, X. Sugar-based triboelectric nanogenerators for effectively harvesting vibration energy and sugar quality assessment. *Nano Energy* **2021**, *88*, 106196. [CrossRef]
25. Ma, P.; Zhu, H.; Lu, H.; Zeng, Y.; Zheng, N.; Wang, Z.L.; Cao, X. Design of biodegradable wheat-straw based triboelectric nanogenerator as self-powered sensor for wind detection. *Nano Energy* **2021**, *86*, 106032. [CrossRef]
26. Zhu, J.; Zhu, M.; Shi, Q.; Wen, F.; Liu, L.; Dong, B.; Haroun, A.; Yang, Y.; Vachon, P.; Guo, X.; et al. Progress in TENG technology—A journey from energy harvesting to nanoenergy and nanosystem. *EcoMat* **2020**, *2*, e12058. [CrossRef]
27. Liu, J.; Huang, H.; Zhou, Q.; Wu, C. Self-powered Downhole Drilling Tools Vibration Sensor Based on Triboelectric Nanogenerator. *IEEE Sens. J.* **2021**, *22*, 2250–2258. [CrossRef]
28. Wang, Y.; Wu, C.; Yang, S. A self-powered rotating speed sensor for downhole motor based on triboelectric nanogenerator. *IEEE Sens. J.* **2020**, *21*, 4310–4316. [CrossRef]
29. Lee, J.W.; Jeong, J.; Yoo, D.; Lee, K.; Lee, S.; Kim, D.S.; Sim, J.Y.; Hwang, W. Pump drill-integrated triboelectric nanogenerator as a practical substitute for batteries of intermittently used devices. *Nano Energy* **2019**, *56*, 612–618. [CrossRef]